

Gyrokinetic Vlasov Code Including Full Three-dimensional Geometry of Experiments

Masanori NUNAMI¹⁾, Tomo-Hiko WATANABE^{1,2)} and Hideo SUGAMA^{1,2)}

¹⁾*National Institute for Fusion Science, Toki 509-5292, Japan*

²⁾*The Graduate University for Advanced Studies (SOKENDAI), Toki 509-5292, Japan*

(Received 23 February 2010 / Accepted 17 March 2010)

A new gyrokinetic Vlasov simulation code, GKV-X, is developed for investigating the turbulent transport in magnetic confinement devices with non-axisymmetric configurations. Effects of the magnetic surface shapes in three-dimensional equilibrium obtained from the VMEC code are accurately incorporated. Linear simulations of ion temperature gradient (ITG) instabilities and zonal flows in the Large Helical Device (LHD) [O. Motojima, N. Oyabu, A. Komori *et al.*, Nucl. Fusion **43**, 1674 (2003)] configuration are carried out by the GKV-X code as benchmark tests against the GKV code [T.-H. Watanabe and H. Sugama, Nucl. Fusion **46**, 24 (2006)]. For high poloidal wavenumbers, the frequency, growth rate, and mode structure of the ITG instability are influenced by the VMEC geometrical data such as the metric tensor components of the Boozer coordinates, while the difference between the zonal flow responses obtained by the GKV and GKV-X codes is found to be small in the core LHD region.

© 2010 The Japan Society of Plasma Science and Nuclear Fusion Research

Keywords: gyrokinetic simulation, ITG mode, zonal flow, LHD, VMEC equilibrium

DOI: 10.1585/pfr.5.016

1. Introduction

Anomalous transport of particles, momentum, and heat is commonly observed in fusion plasma experiments, and has been a central issue in magnetic fusion research for the last few decades. The anomalous transport is considered to be driven by the drift-wave plasma turbulence [1], e.g., the ion temperature gradient (ITG) turbulence. The zonal flows are known to play a critical role in regulating the turbulent transport in toroidal plasmas, and various studies on the zonal flows have been conducted for tokamaks and stellarator/heliotron configurations [2–4].

To explore the zonal flow and microturbulence in non-axisymmetric configurations, a number of linear and non-linear gyrokinetic simulations have been performed [5–9]. In our previous studies [6, 10], we investigated the effects of single and multiple helicity magnetic field configurations on the ITG turbulence in the helical system using the gyrokinetic Vlasov flux-tube code, GKV [11]. The simulation results indicate that a neoclassically optimized (inward-shifted) helical configuration causes a reduction in the ion heat transport through the enhancement of the zonal flows as compared with that in the standard configuration. This is also qualitatively consistent with the Large Helical Device (LHD) [12] experimental results, which indicate that the anomalous transport in the inward-shifted cases is reduced with a decrease in the radial drift of ripple-trapped particles [13], but with an increase in the unfavorable field line curvature [14].

To understand anomalous transport physics better, quantitative comparisons between the gyrokinetic simulations and experiments are required. In the GKV simulations, the model helical fields including limited number of helical Fourier components are employed with the large aspect ratio approximation to the field geometry, where the Jacobian is assumed to be a constant on the flux surface, and diagonal metric tensor components derived from the cylindrical approximation are used. For more quantitative gyrokinetic simulations, it is a natural path to furnish a well-established gyrokinetic code with detailed geometrical information obtained from three-dimensional equilibrium calculations as in Refs. [15–17]. Based on this motivation, we developed a new gyrokinetic Vlasov code, GKV-X. The GKV-X code precisely deals with realistic magnetic configurations, using all the geometrical information provided by the VMEC code [18], which is a standard magnetohydrodynamic equilibrium solver for non-axisymmetric systems. Using the GKV-X code, we investigate the effects of full geometry of the LHD plasmas on the linear ITG mode and the zonal flow response [6, 19–23] by the benchmark tests against the GKV calculation.

The rest of this paper is organized as follows. In Sec. 2, we summarize the field representation and geometry in flux coordinate system. In Sec. 3, we describe basic equations employed in the GKV and GKV-X codes, and clarify the differences between the codes for concrete representations of each term in the equations. In Sec. 4, simulation results of the linear ITG instability and the zonal flow response are compared for both the codes to inves-

author's e-mail: nunami.masanori@nifs.ac.jp

tigate the effects of the metric tensor and the Jacobian in helical systems. Section 5 presents the conclusions of the study.

2. Magnetic Field Geometry

The detailed expressions of the magnetic field representation and geometry in the flux coordinate system are described here. We consider the flux coordinate system $\{\rho, \theta, \zeta\}$, where θ and ζ are poloidal and toroidal angles, respectively. The labeling index of the flux surfaces, $\rho \equiv \sqrt{\Psi/\Psi_a}$, is a dimensionless quantity. Here Ψ represents the toroidal magnetic flux with the minor radius, r , defined by $\Psi = B_{\text{ax}} r^2/2$, with a field strength at the magnetic axis, B_{ax} , and Ψ_a is the value of the toroidal flux at the last closed surface. Therefore, the flux label can be represented as $\rho = r/a$, where a denotes the minor radius of the last closed surface defined by $\Psi_a = B_{\text{ax}} a^2/2$ at $\rho = 1$.

2.1 Field representation

Let us consider the Boozer coordinates [24] $\{\rho, \theta_B, \zeta_B\}$ as the flux coordinate system. The contravariant representation of the magnetic field in the Boozer coordinates, is written as

$$\begin{aligned} \mathbf{B} &= \nabla\Psi(\rho) \times \nabla\theta_B + q^{-1}(\rho)\nabla\zeta_B \times \nabla\Psi(\rho) \\ &= \frac{\Psi'}{\sqrt{g_B}} (\mathbf{e}_{\zeta_B} + q^{-1}(\rho)\mathbf{e}_{\theta_B}) \\ &= B^{\zeta_B} \mathbf{e}_{\zeta_B} + B^{\theta_B} \mathbf{e}_{\theta_B}, \end{aligned} \quad (1)$$

where, $\mathbf{e}_{\theta_B} \equiv \partial\mathbf{r}/\partial\theta_B$, $\mathbf{e}_{\zeta_B} \equiv \partial\mathbf{r}/\partial\zeta_B$, $q(\rho)$ is the safety factor and $\sqrt{g_B}$ is the Jacobian in the coordinate system,

$$\begin{aligned} \sqrt{g_B} &= (\nabla\rho \times \nabla\theta_B \cdot \nabla\zeta_B)^{-1} \\ &= \frac{\Psi'}{B^2} (B_{\zeta_B} + q^{-1}(\rho)B_{\theta_B}), \end{aligned} \quad (2)$$

where the prime symbol represents the derivative with respect to the flux label ρ , i.e., $A' = dA/d\rho$. Hereafter, for the sake of simplicity, the subscript ‘‘B’’ of the poloidal and toroidal angles is omitted when the angles are used as subscripts of any variables, e.g., B_{θ_B} is represented as B_θ . The poloidal and toroidal covariant components of the field, B_θ and B_ζ , are flux functions in the Boozer coordinates and consist of the covariant representation of the field written as

$$\mathbf{B} = B_\rho \nabla\rho + B_\theta \nabla\theta_B + B_\zeta \nabla\zeta_B. \quad (3)$$

The components of the equilibrium field B_θ , B_ζ , B^θ , and B^ζ are directly given by the VMEC code except for the component B_ρ . The radial covariant component, B_ρ , can be determined using the contravariant components,

$$B_\rho = B^\theta g_{\theta\rho} + B^\zeta g_{\zeta\rho}. \quad (4)$$

Here, $g_{\theta\rho}$ and $g_{\zeta\rho}$ are the covariant components of the metric tensor.

2.2 Metric components

Since the VMEC code uses the original coordinate system, the ‘‘VMC coordinates,’’ we need to convert the

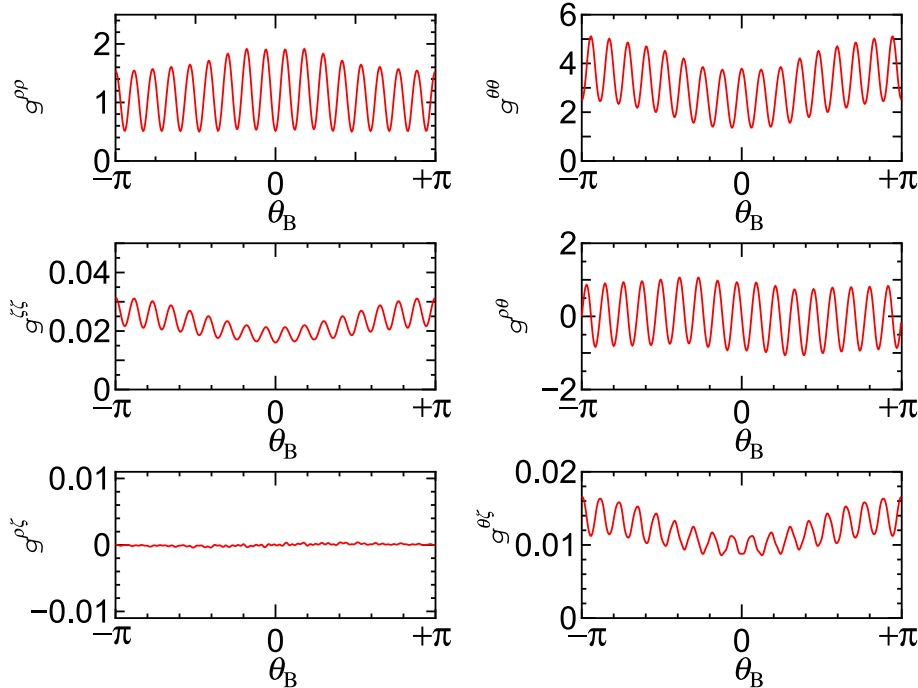


Fig. 1 Example of contravariant components of metric tensor, used for k_\perp in Eq. (26), obtained by the VMEC/NEWBOZ outputted configuration at $\rho = 0.6$ in the Boozer coordinate system $\{\rho, \theta_B, \zeta_B\}$ with a fixed $\alpha = \zeta_B - q_0\theta_B$. Each component is in units of a^{-2} .

coordinates into the Boozer coordinates; thus, we use the NEWBOZ code [25], which transforms coordinates from the VMEC to the Boozer coordinates $\{\rho, \theta_B, \zeta_B\}$ with the radial flux label ρ . The VMEC/NEWBOZ code package provides information about the shapes of the flux surfaces defined in the cylindrical coordinates $\{R, Z, \phi\}$ as Fourier series for θ_B and ζ_B ,

$$R = \sum_k R_k(\rho) \cos(n_k \zeta_B - m_k \theta_B), \quad (5a)$$

$$Z = \sum_k Z_k(\rho) \sin(n_k \zeta_B - m_k \theta_B), \quad (5b)$$

$$\phi = \zeta_B + \sum_k \phi_k(\rho) \sin(n_k \zeta_B - m_k \theta_B). \quad (5c)$$

From Eq. (5), the covariant metric components can be obtained as follows:

$$g_{ij} = \frac{\partial R}{\partial i} \frac{\partial R}{\partial j} + \frac{\partial Z}{\partial i} \frac{\partial Z}{\partial j} + R^2 \frac{\partial \phi}{\partial i} \frac{\partial \phi}{\partial j}, \quad (6)$$

where $i, j = \{\rho, \theta_B, \zeta_B\}$. Using Eqs. (1), (2) and (3), $g_{\theta\zeta}$ and $g_{\zeta\zeta}$ can also be represented as

$$g_{\theta\zeta} = \frac{\sqrt{g_B}}{\Psi'} B_\theta - q^{-1}(\rho) g_{\theta\theta}, \quad (7a)$$

$$g_{\zeta\zeta} = \frac{\sqrt{g_B}}{\Psi'} B_\zeta - q^{-1}(\rho) g_{\theta\zeta}, \quad (7b)$$

which are useful for a consistency check on the calculation of the metric tensor. We can obtain the contravariant metric components from the covariant ones as given below:

$$g^{il} = \frac{1}{g_B} (g_{jm} g_{kn} - g_{jn} g_{km}), \quad (8)$$

where $\{i, j, k\}$ and $\{l, m, n\}$ are even permutations of $\{\rho, \theta_B, \zeta_B\}$. As an example, Fig. 1 shows the contravariant components of the metric tensor in the standard LHD equilibrium at the flux label $\rho = 0.6$, where g^{ij} for $i, j = \{\rho, \theta_B, \zeta_B\}$, calculated from the VMEC/NEWBOZ output, are plotted along the field line.

3. GKV and GKV-X Codes

In this section, we present the gyrokinetic equation employed in the GKV and GKV-X codes as well as concrete expressions of each term in which profiles along the field line are compared for both the codes.

3.1 Basic equations

Let $\{r, \theta, \zeta\}$ be a generalized flux coordinate system. The local flux-tube model [26] with the field-aligned coordinates $\{x, y, z\}$ is used in the codes, where $x = r - r_0$, $y = (r_0/q_0)[q(\rho)\theta - \zeta]$ and $z = \theta$, with the safety factor q_0 at the minor radius $r_0 = \rho_0 a$. The minor radius, r_0 , is defined by the toroidal magnetic flux $\Psi(r = r_0) = B_{ax} r_0^2/2$. Both the codes solve the electrostatic gyrokinetic equation of the perturbed ion gyrocenter distribution function δf [11, 27],

$$\frac{\partial \delta f}{\partial t} + v_{\parallel} \mathbf{b} \cdot \nabla \delta f + \frac{c}{B_0} \mathbf{b} \times \nabla \Phi \cdot \nabla \delta f$$

$$+ \mathbf{v}_d \cdot \nabla \delta f - \frac{\mu}{m_i} \mathbf{b} \cdot \nabla B \frac{\partial \delta f}{\partial v_{\parallel}} = (\mathbf{v}_* - \mathbf{v}_d - v_{\parallel} \mathbf{b}) \cdot \frac{e \nabla \Phi}{T_i} F_M + C(\delta f), \quad (9)$$

where $\mathbf{b} = \mathbf{B}/B$ is the unit vector parallel to the magnetic field, and v_{\parallel} and $\mu = m_i v_{\perp}^2/2B$, regarded as the velocity-space coordinates in the codes, denote the parallel velocity and magnetic moment, respectively. The Maxwellian distribution with temperature T_i and the collision term are denoted by F_M and $C(\delta f)$, respectively. The magnetic drift velocity is $\mathbf{v}_d = (c/eB) \mathbf{b} \times (\mu \nabla B + m_i v_{\parallel}^2 \mathbf{b} \cdot \nabla \mathbf{b})$ and the diamagnetic drift velocity is $\mathbf{v}_* = (cT_i/eB) \mathbf{b} \times [\nabla \ln n + (m_i v^2/2T_i - 3/2) \nabla \ln T_i]$. The perpendicular wavenumber vector is defined by

$$\mathbf{k}_{\perp} = k_x \nabla r + k_y \nabla \left[\frac{r_0}{q_0} (q(r)\theta - \zeta) \right]. \quad (10)$$

In the wavenumber space, (k_x, k_y) , the average electrostatic potential at the gyrocenter, Φ , is related to the electrostatic potential at the particle position, ϕ , as $\Phi_{k_x, k_y} = J_0(k_{\perp} v_{\perp}/\Omega_i) \phi_{k_x, k_y}$. The zeroth-order Bessel function, $J_0(k_{\perp} v_{\perp}/\Omega_i)$, represents the finite gyroradius effect, where the ion gyro frequency is defined by $\Omega_i = eB/m_i c$. The electrostatic potential ϕ_{k_x, k_y} is calculated from the quasi-neutrality condition

$$\int d^3 v J_0 \delta f_{k_x, k_y} - n_0 \frac{e \phi_{k_x, k_y}}{T_i} [1 - \Gamma_0(b)] = n_{e, k_x, k_y}, \quad (11)$$

where $\delta f_{k_x, k_y}$ is the Fourier component of δf , $\Gamma_0(b) = e^b I_0(b)$, with $b = (k_{\perp} v_{ti}/\Omega_i)^2$, and I_0 is the modified zeroth-order Bessel function. The ion thermal speed is defined by $v_{ti} = \sqrt{T_i/m_i}$. The electron density perturbation, n_{e, k_x, k_y} , is assumed to be adiabatic and is given in terms of the electron temperature, T_e , and the averaged density, n_0 , as

$$\frac{n_{e, k_x, k_y}}{n_0} = \begin{cases} e [\phi_{k_x, k_y} - \langle \phi_{k_x, k_y} \rangle] / T_e & \text{if } k_y = 0, \\ e \phi_{k_x, k_y} / T_e & \text{if } k_y \neq 0. \end{cases} \quad (12)$$

Also, $\langle \dots \rangle$ indicates the flux surface average defined as

$$\langle A(z) \rangle = \int_{-\infty}^{\infty} \sqrt{g_F} A(z) dz / \int_{-\infty}^{\infty} \sqrt{g_F} dz, \quad (13)$$

for an arbitrary function of z , $A(z)$. Here, $\sqrt{g_F}$ is the Jacobian in the coordinate system $\{x, y, z\}$, which is related to the Jacobian in the Boozer coordinates, as shown in Eq. (2):

$$\sqrt{g_F} = \frac{q_0}{ar_0} \sqrt{g_B}. \quad (14)$$

We adopt the modified periodic boundary condition at the boundaries of the flux-tube domain [26]. In linear and collisionless case, the Fourier transformed expression of Eq. (9) becomes

$$\left(\frac{\partial}{\partial t} + v_{\parallel} \mathbf{b} \cdot \nabla - \frac{\mu}{m_i} \mathbf{b} \cdot \nabla B \frac{\partial}{\partial v_{\parallel}} + i\omega_{Di} \right) \delta f_{k_x, k_y}$$

$$= F_M(-v_{\parallel} \mathbf{b} \cdot \nabla - i\omega_{\text{Di}} + i\omega_{*T_i}) J_0(k_{\perp} \rho_i) \frac{e\phi_{k_x, k_y}}{T_i}, \quad (15)$$

where $\omega_{\text{Di}} = \mathbf{k}_{\perp} \cdot \mathbf{v}_d$ and $\omega_{*T_i} = \mathbf{k}_{\perp} \cdot \mathbf{v}_*$ are the magnetic and diamagnetic drift frequencies, respectively, and the ion gyroradius is defined by $\rho_i = v_{\perp}/\Omega_i$.

3.2 Geometrical expressions used in GKV

In the GKV simulations for helical configurations such as the LHD, we employed a model field configuration,

$$B = B_0 \left[1 - \epsilon_{00}(r) - \epsilon_t(r) \cos \theta - \sum_{l=L-1}^{L+1} \epsilon_l(r) \cos[l\theta - M\zeta] \right], \quad (16)$$

which includes the toroidal ϵ_t , the main helicity $\epsilon_h = \epsilon_L$, and two side-band helical components $\epsilon_+ = \epsilon_{L+1}$ and $\epsilon_- = \epsilon_{L-1}$. Here, M and L indicate the main period numbers of the confinement field in the toroidal and poloidal directions, respectively. For the LHD, $L = 2$ and $M = 10$. Here, we regard the poloidal angle θ as a coordinate along the field line labeled by $\alpha = \zeta - q_0\theta = \text{constant}$. In the GKV code, we use the large aspect ratio approximation for the confinement field geometry assuming the presence of small helical ripples and cylindrical diagonal metric tensor [7, 8]. Under the approximation, in terms of the field-aligned coordinates $\{x, y, z\}$, the magnetic drift frequency on the right-hand side of Eq. (15) is given by

$$\begin{aligned} \omega_{\text{Di}} = & -\frac{c}{e} \left(\mu + \frac{1}{B} m_i v_{\parallel}^2 \right) \frac{\epsilon_t}{r_0} \left[k_y \left(\frac{\rho_0 \epsilon'_{00}}{\epsilon_t} + \frac{\rho_0 \epsilon'_t}{\epsilon_t} \cos z \right. \right. \\ & \left. \left. + \sum_{l=L-1}^{L+1} \frac{\rho_0 \epsilon'_l}{\epsilon_t} \cos[(l - Mq_0)z - M\alpha] \right) \right. \\ & \left. + (k_x + \hat{s}z k_y) \left(\sin z + \sum_{l=L-1}^{L+1} l \frac{\epsilon_l}{\epsilon_t} \sin[(l - Mq_0)z - M\alpha] \right) \right], \end{aligned} \quad (17)$$

using Eq. (16) for a fixed α . Here, $\hat{s} = (r_0/q_0)dq/dr = (\rho_0/q_0)q'$ is the magnetic shear parameter and is assumed to be constant, and $\epsilon' = d\epsilon/d\rho = a(d\epsilon(r)/dr)$. The diamagnetic drift frequency is expressed as

$$\omega_{*T_i} = -\frac{cT_i}{eB_0 L_n} k_y \left[1 + \eta_i \left(\frac{m_i v^2}{2T_i} - \frac{3}{2} \right) \right], \quad (18)$$

where $\eta_i = L_n/L_T$ with the background gradients for density $L_n^{-1} = -d \ln n/dr$, and for temperature $L_T^{-1} = -d \ln T_i/dr$. The perpendicular wavenumber k_{\perp} is written as

$$k_{\perp}^2 = (k_x + \hat{s}z k_y)^2 + k_y^2, \quad (19)$$

which is used for the zeroth-order Bessel function in Eq. (15) and the zeroth-order modified Bessel function in Eq. (11). The parallel derivative in Eq. (15) is given by

$$\mathbf{b} \cdot \nabla = \frac{1}{R_0 q_0} \frac{\partial}{\partial z}, \quad (20)$$

where the safety factor, q_0 , and the major radius, R_0 , are regarded as constant. This corresponds to the approximation that the Jacobian is expressed as $\sqrt{g_F} \propto 1/(\mathbf{B} \cdot \nabla \theta) \propto 1/B$, i.e., $B\sqrt{g_F}$ is a constant on the flux surface. This implies that the coordinates in this model do not coincide exactly with the Boozer coordinates. In the large aspect ratio approximation, however, the difference is negligible. The flux surface average for the arbitrary function, $A(z)$, in Eq. (13) reduces to

$$\langle A(z) \rangle = \int_{-\infty}^{\infty} A(z) dz / B \Big| \int_{-\infty}^{\infty} dz / B, \quad (21)$$

which guarantees the property $\langle \mathbf{B} \cdot \nabla A \rangle = 0$. According to the approximation, the parallel derivative of B , which is employed for the mirror force term in Eq. (15), can be written as

$$\begin{aligned} \mathbf{b} \cdot \nabla B &= \frac{B_0 \epsilon_t}{R_0 q_0} \left(\sin z + \sum_{l=L-1}^{L+1} (l - Mq_0) \frac{\epsilon_l}{\epsilon_t} \sin[(l - Mq_0)z - M\alpha] \right), \end{aligned} \quad (22)$$

with the constant field line label α .

3.3 Geometrical expressions used in GKV-X

In the GKV-X code, we employ the same basic equations as that in the GKV code, i.e., Eqs. (9) and (11), but using the confinement field model obtained by the VMEC/NEWBOZ code package that gives an output of the confinement field strength in terms of the Fourier series in the Boozer coordinate system $\{\rho, \theta_B, \zeta_B\}$ as follows:

$$\begin{aligned} B = & \sum_{n=0}^{n_{\max}} B_{0,n}(\rho) \cos n\zeta_B \\ & + \sum_{m=1}^{m_{\max}} \sum_{n=-n_{\max}}^{n_{\max}} B_{m,n}(\rho) \cos[m\theta_B - n\zeta_B], \end{aligned} \quad (23)$$

where $B_{m,n}(\rho)$ is the Fourier component with the poloidal (m) and toroidal (n) mode numbers. Here, m_{\max} and n_{\max} are the maximum mode numbers for the poloidal and toroidal directions used in the VMEC calculation, respectively. Furthermore, in the GKV-X, we implement exact representations of each term in Eq. (9) with full geometrical factors, the Jacobian and the metric tensor. In the coordinates $\{\rho, \theta_B, \zeta_B\}$, the magnetic drift frequency in Eq. (15) with zero-beta, $\mathbf{b} \cdot \nabla \mathbf{b} = (\nabla_{\perp} B)/B$, is given by

$$\begin{aligned} \omega_{\text{Di}} = & -\frac{c}{eB^2} \frac{a}{\sqrt{g_B}} \left(\mu + \frac{1}{B} m_i v_{\parallel}^2 \right) \left[k_y \left[\left(\frac{\rho_0}{q_0} B_{\rho} + \hat{s}\theta_B B_{\zeta} \right) \frac{\partial B}{\partial \theta_B} \right. \right. \\ & \left. \left. + (\rho_0 B_{\rho} - \hat{s}\theta_B B_{\theta}) \frac{\partial B}{\partial \zeta_B} - \left(\frac{\rho_0}{q_0} B_{\theta} + \rho_0 B_{\zeta} \right) \frac{\partial B}{\partial \rho} \right] \right. \\ & \left. + k_x \left[B_{\zeta} \frac{\partial B}{\partial \theta_B} - B_{\theta} \frac{\partial B}{\partial \zeta_B} \right] \right], \end{aligned} \quad (24)$$

with the perpendicular wavenumbers, k_x and k_y , where the field-aligned coordinates $\{x, y, z\}$, for the GKV-X case are

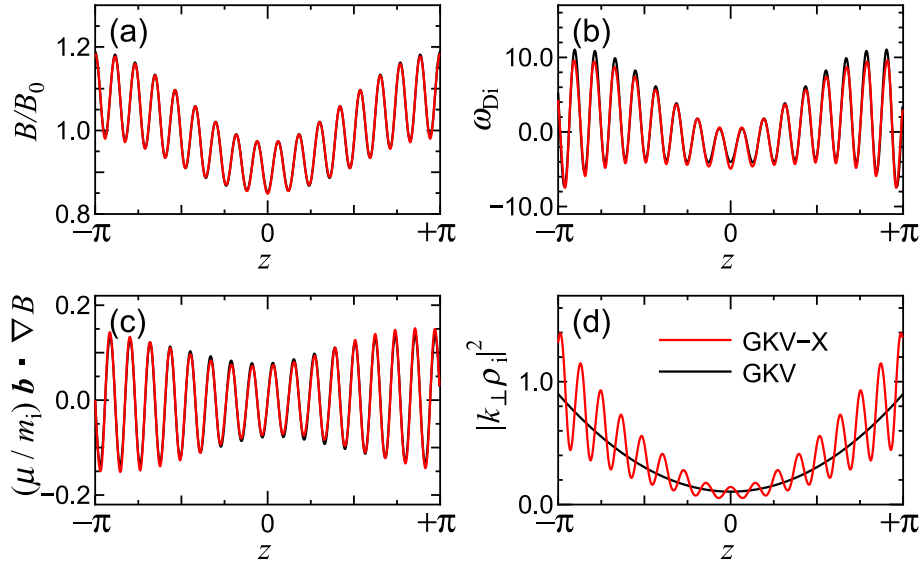


Fig. 2 Profiles of (a) normalized magnetic field strength B/B_0 , (b) magnetic drift frequency ω_{Di} normalized by $v_i L_n^{-1}$, (c) mirror force term normalized by $v_i^2 L_n^{-1}$, and (d) square of the normalized perpendicular wavenumber, $k_\perp \rho_i$. All profiles are evaluated at $\rho = 0.6$, and three plots except for (a) are calculated for $k_x \rho_i = 0$ and $k_y \rho_i = 0.324$. In (b) and (c), the magnetic moment is $\mu / (m_i \Omega_i B^{-1}) = 0.50 v_i L_n$. Black and red curves show the results of the GKV and GKV-X codes, respectively.

defined later. The diamagnetic drift frequency can also be expressed as

$$\begin{aligned} \omega_{*Ti} &= -\frac{cT_i}{eL_n} \frac{\rho_0 a^2}{q_0 B^2 \sqrt{g_B}} (B_\theta + q_0 B_\zeta) k_y \left[1 + \eta_i \left(\frac{m_i v^2}{2T_i} - \frac{3}{2} \right) \right] \\ &= -\frac{cT_i}{eL_n} \frac{\rho_0 a^2}{\Psi'} k_y \left[1 + \eta_i \left(\frac{m_i v^2}{2T_i} - \frac{3}{2} \right) \right], \end{aligned} \quad (25)$$

where we use Eq. (2) in the last line. Using the identity for the contravariant components of the metric tensor (Eq. (8)), we can obtain the perpendicular wavenumber k_\perp as follows:

$$\begin{aligned} k_\perp^2 &= k_x^2 a^2 g^{\rho\rho} + 2k_x k_y a^2 \left[\hat{s} \theta_B g^{\rho\rho} + \frac{\rho_0}{q_0} (q_0 g^{\rho\theta} - g^{\rho\zeta}) \right] \\ &\quad + k_y^2 a^2 \left[\frac{\rho_0^2}{q_0^2} (g^{\zeta\zeta} + q_0^2 g^{\theta\theta} - 2q_0 g^{\theta\zeta}) \right. \\ &\quad \left. + 2\hat{s} \theta_B \frac{\rho_0}{q_0} (q_0 g^{\rho\theta} - g^{\rho\zeta}) + \hat{s}^2 \theta_B^2 g^{\rho\rho} \right]. \end{aligned} \quad (26)$$

The parallel derivative is given as

$$\mathbf{b} \cdot \nabla = \frac{\Psi'}{q_0 B \sqrt{g_B}} \left(\frac{\partial}{\partial \theta_B} + q_0 \frac{\partial}{\partial \zeta_B} \right), \quad (27)$$

with the Jacobian Eq. (2). Therefore, in the GKV-X code, we use Eq. (13) as the flux surface averaging, and the parallel derivative of B can be represented as

$$\begin{aligned} \mathbf{b} \cdot \nabla B &= \frac{\Psi'}{q_0 B \sqrt{g_B}} \sum_{m=1}^{m_{\max}} \sum_{n=-n_{\max}}^{n_{\max}} B_{m,n}(\rho) (m - n q_0) \sin[n \zeta_B - m \theta_B]. \end{aligned} \quad (28)$$

For the benefit of comparing the magnetic drift frequencies (Eqs. (17) and (24)), we write down the concrete forms of the derivatives of the field strength along each direction in the coordinates $\{\rho, \theta_B, \zeta_B\}$ as follows:

$$\begin{aligned} \frac{\partial B}{\partial \rho} &= \sum_{n=0}^{n_{\max}} B'_{0,n}(\rho) \cos n \zeta_B \\ &\quad + \sum_{m=1}^{m_{\max}} \sum_{n=-n_{\max}}^{n_{\max}} B'_{m,n}(\rho) \cos[m \theta_B - n \zeta_B], \end{aligned} \quad (29a)$$

$$\frac{\partial B}{\partial \theta_B} = -\sum_{m=1}^{m_{\max}} \sum_{n=-n_{\max}}^{n_{\max}} B_{m,n}(\rho) m \sin[m \theta_B - n \zeta_B], \quad (29b)$$

$$\begin{aligned} \frac{\partial B}{\partial \zeta_B} &= -\sum_{n=0}^{n_{\max}} B_{0,n}(\rho) n \sin n \zeta_B \\ &\quad + \sum_{m=1}^{m_{\max}} \sum_{n=-n_{\max}}^{n_{\max}} B_{m,n}(\rho) n \sin[m \theta_B - n \zeta_B]. \end{aligned} \quad (29c)$$

In the GKV-X code, we use the above mentioned terms after converting the coordinates into the field-aligned coordinates $\{x, y, z\}$ with the relations, $x = a(\rho - \rho_0)$, $y = (a\rho_0/q_0)(q\theta_B - \zeta_B)$, and $z = \theta_B$ in a constant field line label $\alpha = \zeta_B - q_0 \theta_B$. The parallel derivative in Eq. (27), for example, is written as $\mathbf{b} \cdot \nabla = (\Psi'/q_0 B \sqrt{g_B})(\partial/\partial z)$. The concrete profiles of each term in Eq. (15), which are used in the GKV and GKV-X simulations, are shown in Fig. 2. The profiles are discussed in detail in the following section.

4. Comparison of Simulation Results

To investigate the effects of non-axisymmetric geometry on the ITG modes and zonal flows, gyrokinetic Vlasov simulations using linearized versions of the GKV-X and

Table 1 Parameters at flux surface $\rho = 0.6$ employed in the GKV code. The prime symbol indicates $A' = dA/d\rho$.

q_0	r_0/R_0	ϵ_t	ϵ_h/ϵ_t	ϵ_-/ϵ_t	ϵ_+/ϵ_t
1.9	0.0907	0.0878	0.9113	-0.2806	0.0498
\hat{s}	$\rho_0\epsilon'_{00}/\epsilon_t$	$\rho_0\epsilon'_t/\epsilon_t$	$\rho_0\epsilon'_h/\epsilon_t$	$\rho_0\epsilon'_-/\epsilon_t$	$\rho_0\epsilon'_+/\epsilon_t$
-0.87501	0.1997	1.006	1.9486	-0.6452	0.070

GKV codes are performed in a way similar to that in Refs. [7] and [11]. Here, we use the magnetic configuration with the parameters of the confinement field based on the VMEC calculation results for the standard LHD case, which is similar to the ‘‘S-B case’’ in Ref. [8]. In the GKV-X simulation, we use the VMEC configuration with full helical components. On the other hand, the GKV calculation uses the parameters summarized in Table 1, which are obtained from the VMEC configuration in terms of the toroidal, main helical, two side-band components, and their radial derivatives. In both the calculations, we use the same parameters for the variables, $\eta_i = 3$, $T_e/T_i = 1$, $L_n/R_0 = 0.3$, $q_0 = 1.9$, $\hat{s} = -0.87501$, and $\alpha = 0$.

4.1 Effects of full geometry

To highlight the differences in the effects of the metric tensor, Jacobian, and full Fourier components of the confinement field between the two models, we plot profiles of each term in Eq. (15), concrete expressions of which were described in the previous section. In Fig. 2, we plot the normalized field strength; the magnetic drift frequency, ω_{Di} , normalized by $v_{ti}L_n^{-1}$; the mirror force term, $(\mu/m_i)\mathbf{b} \cdot \nabla B$, normalized by $v_{ti}^2L_n^{-1}$; and the square of the normalized perpendicular wavenumber, $k_\perp\rho_i$, as functions of the field-aligned coordinate z at $\rho = 0.6$. Here, to normalize the field strength, we use $B_{0,0}(\rho)$ as the normalization factor B_0 . As seen in the figures, the profiles of the field strength, magnetic drift frequency, and mirror force term for the GKV-X and GKV codes appear similar to each other. However, in the region near $z = 0$, where the ITG instabilities are stronger because of more unfavorable magnetic field line curvature, a difference in the magnitude of the magnetic drift frequencies is not negligible and in fact, causes a difference in the ITG-mode growth rates. For the diamagnetic drift frequency given in Eqs. (18) and (25), we observe that there is only a small difference by the factor of $\omega_{*Ti}^{(GKV)}/\omega_{*Ti}^{(GKV-X)} = \Psi'/(a^2\rho_0B_0) \approx 1.0097$. The profiles of the perpendicular wavenumber show a clear difference due to the effects of the helical ripples on the metric tensor. In the following simulations for the linear ITG modes and collisionless damping of the zonal flows, we obtain the results at $\rho = 0.6$, which is in the core plasma region of the LHD.

4.2 Linear ITG instability

Figure 3 shows the growth rates and real frequencies

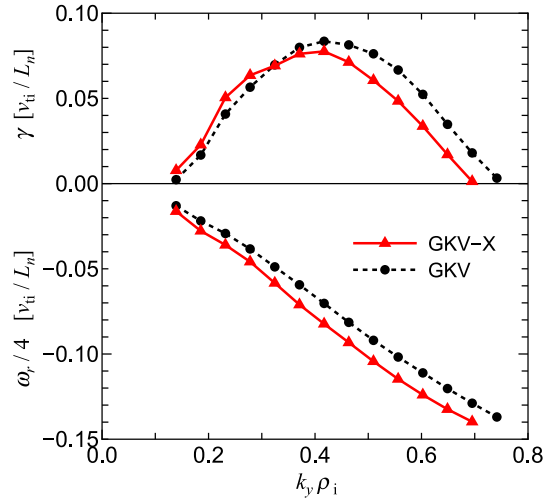


Fig. 3 Growth rates γ (top) and real frequencies ω_r (bottom) of the linear ITG mode, as functions of the normalized poloidal wavenumber, $k_y\rho_i$, for the GKV simulation (black dashed lines with circles) and the GKV-X simulation (red solid lines with triangles).

of the linear ITG instability, obtained from the GKV-X and GKV simulations for $\rho = 0.6$, as functions of the normalized poloidal wavenumber, $k_y\rho_i$, where $k_x = 0$ is used. The growth rate in the GKV-X calculation, compared to that in the GKV, is slightly higher for $k_y\rho_i \lesssim 0.3$ and lower for $k_y\rho_i \gtrsim 0.3$. The real frequency obtained by the GKV-X simulation is slightly more negative than that by the GKV simulation. The differences between the codes are magnified with the increasing poloidal wavenumber, which originates from the ripple components and full metric tensor through the magnetic drift frequency (ω_{Di}) and perpendicular wavenumber (k_\perp), respectively. Because more helical ripple components are included in the magnetic drift frequency for the GKV-X case, the difference of ω_{Di} appears as shown in Fig. 2-(b); that is, ω_{Di} for the GKV-X is more negative than for the GKV around $z \approx 0$, where the ITG instabilities are strongly driven by unfavorable magnetic field line curvature. According to Eq. (24), the difference in ω_{Di} is enhanced in the large $|k_y|$ region. In the expression of the perpendicular wavenumber (Eq. (26)), the terms including the metric tensor components $g^{\theta\theta}$ and $g^{\rho\rho}$, which reflect the shape of the elliptic magnetic surface, are influential in k_\perp related to the finite gyroradius effect. The term with $g^{\theta\theta}$ remains finite around $z \approx 0$, and the contribution of the term to k_\perp is also enhanced for higher poloidal wavenumbers, while the term with $g^{\rho\rho}$ vanishes at $z = 0$. In the other terms of Eq. (15), i.e., the diamagnetic drift frequency and the mirror force term, the differences between the codes are much smaller than those in ω_{Di} and k_\perp . Therefore, at large poloidal wavenumbers, the helical ripple components of the confinement field and the metric tensor of the magnetic surface affect the frequency and the growth rate of the ITG instability through the magnetic

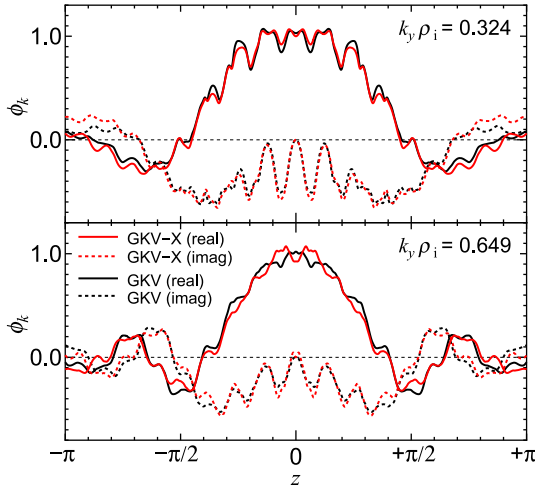


Fig. 4 Eigenfunctions of electrostatic potential $\phi_k = \phi_r + i\phi_i$ along the parallel-to-field coordinate z for linear ITG modes for $k_y \rho_i = 0.324$ (top) and $k_y \rho_i = 0.649$ (bottom) at $k_x = 0$. Real and imaginary parts of the eigenfunctions are plotted by solid and dashed curves, respectively. Red and black curves express the results of the GKV-X and GKV codes, respectively.

drift frequency and the finite gyroradius effect.

Eigenfunctions of the ITG modes are also investigated (Fig. 4) for $k_y \rho_i = 0.324$ and $k_y \rho_i = 0.649$. As seen in the plot for $k_y \rho_i = 0.324$, the mode structures of ϕ_k obtained by the two codes have a similar profile, which is accompanied by oscillations associated with the helical ripples. In contrast, the field-aligned profiles of ϕ_k for larger poloidal wavenumber $k_y \rho_i = 0.649$ show different ripple structures in the unfavorable curvature region around $z \simeq 0$. This is consistent with the results of the growth rate and the real frequency shown in Fig. 3, where the differences are found mainly in the higher poloidal wavenumbers. Linear eigenvalue analysis [28–30] also predicts a similar mode structure to the present results.

4.3 Zonal flow evolution

The zonal flows are produced by an electrostatic field perturbation varying in the radial direction and have the poloidal wavenumber $k_y = 0$. Hence, the perpendicular wavenumbers in Eqs. (19) and (26) are simply given by

$$k_{\perp}^2 = \begin{cases} k_x^2 & \text{for GKV,} \\ k_x^2 a^2 g^{\rho\rho} & \text{for GKV-X.} \end{cases} \quad (30)$$

Figure 5 shows the time evolution of the flux surface averaged zonal flow potential $\langle \phi_{k_{\perp}} \rangle$ during its linear collisionless damping found in the GKV and GKV-X simulations. The results are shown for two different radial wavenumbers, $k_x \rho_i = 0.0637$ and $k_x \rho_i = 0.1274$. As observed in the plots, the response functions of the zonal flows to the initial perturbation, $\langle \phi_{k_{\perp}}(t) \rangle / \langle \phi_{k_{\perp}}(0) \rangle$ given by the two codes agree well with each other for both k_x values. The residual levels of the zonal flow potentials at $t/(L_n/v_{ti}) = 100$

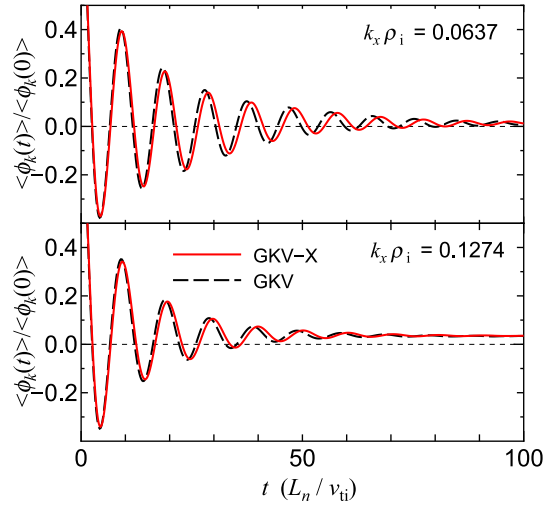


Fig. 5 Linear response of the zonal flow potential to the initial perturbation $\langle \phi_{k_{\perp}}(t) \rangle / \langle \phi_{k_{\perp}}(0) \rangle$ for the GKV simulation with model field (black dashed curves) and GKV-X simulation with VMEC field configuration (red solid curves). Here, the radial wavenumbers are $k_x \rho_i = 0.0637$ (top) and $k_x \rho_i = 0.1274$ (bottom) for both codes.

are obtained as $\mathcal{K}_{\text{GKV-X}} = (1.33 \pm 0.81) \times 10^{-2}$, $\mathcal{K}_{\text{GKV}} = (1.32 \pm 0.79) \times 10^{-2}$ for $k_x \rho_i = 0.0637$, and $\mathcal{K}_{\text{GKV-X}} = (3.54 \pm 0.15) \times 10^{-2}$, $\mathcal{K}_{\text{GKV}} = (3.36 \pm 0.10) \times 10^{-2}$ for $k_x \rho_i = 0.1274$. Thus, the effect of the metric tensor on the residual zonal flow levels is very weak. We consider that this is because the ripple effect of the perpendicular wavenumber given in Eq. (30) for the GKV-X case with $g^{\rho\rho}$, which is plotted in Fig. 1, is blinded with taking the flux surface average to determine the residual zonal flow potential that loses the poloidal-angle-dependent components associated with the geodesic acoustic mode (GAM) oscillations. Regarding the short-time response of the zonal flow potential, the finite gyroradius effects (due to $k_{\perp} \rho_i$) on the frequency and the damping rate of the GAM are weaker than the effects of the Fourier spectrum of the confinement field strength, as theoretically shown in Ref. [31]. In the present paper, the difference between the field strength structures used in the GKV and GKV-X calculations is negligible as seen in Fig. 2-(a). Therefore, the behaviors of the zonal flow response shown by both the codes have only slight differences.

5. Conclusions

In this paper, we report the development of the GKV-X code, which is applicable to non-axisymmetric configuration such as the LHD. This code is designed to accurately deal with the effects of complicated geometry and helical ripple components of the confinement field, while the original GKV code uses the model confinement field for the geometry based on the large aspect ratio approximation. The new code includes full information about

the metric tensor, Jacobian, and Fourier components of the helical field obtained from the VMEC equilibrium calculation. We performed the benchmark test of the GKV-X against the GKV calculations in the core plasma region of the standard LHD configuration. In the simulations of the linear ITG instability, we have found that the effects of full geometry and helical ripples are enhanced for higher poloidal wavenumbers due to the finite gyroradius effect and the magnetic drift frequency. The collisionless damping of the zonal flow potential is also examined, where the geometrical effects on the zonal flow show little difference between both codes. Thus, we can conclude that the GKV calculation with model helical field is useful especially for the phenomena with long wavelengths in the standard LHD configuration, with relatively small helical ripple components. However, we should note that the above mentioned benchmark tests are conducted for a core plasma region at $\rho = 0.6$, where the GKV simulations can be relatively appropriate for the investigation of the ITG modes and zonal flows. Therefore, the GKV-X code can be a powerful tool for examining the effects of the full geometry and helical ripples on the ITG modes and the zonal flows if we extend the simulation region to the edge region of the LHD plasmas where the geometrical effects are expected to appear more remarkably. This is attributed to the strongly distorted magnetic surfaces and more complicated helical ripple components that exist in the edge region.

The gyrokinetic simulation including the full effects of the complicated three-dimensional magnetic field is useful for quantitative investigation of the ITG modes and zonal flows in the helical systems. The GKV-X code enables us to study the ITG modes and zonal flows in various types of field configurations, and to make comparisons with the experimental data, the results of which will be reported elsewhere.

Acknowledgment

The author (M. N.) appreciates Dr. S. Satake for useful information about the LHD equilibrium and the VMEC/NEWBOZ code. This work is supported in part by the Japanese Ministry of Education, Culture, Sports, Science and Technology, Grant No. 21560861, and in part by the NIFS Collaborative Research Program, NIFS09KTAL022, NIFS08KDAD008, NIFS08KTAL006, and NIFS08KNXN14.

- [1] W. Horton, *Rev. Mod. Phys.* **71**, 735 (1999).
- [2] P.H. Diamond, S.-I. Itoh, K. Itoh and T.S. Hahm, *Plasma Phys. Control. Fusion* **47**, R35 (2005).

- [3] K. Itoh, S.-I. Itoh, P.H. Diamond and A. Fujisawa, *Phys. Plasmas* **13**, 055502 (2006).
- [4] A. Fujisawa, *Nucl. Fusion* **49**, 013001 (2009).
- [5] V. Kornilov, R. Kleiber, R. Hatzky, L. Villard and G. Jost, *Phys. Plasmas* **11**, 3196 (2004).
- [6] T.-H. Watanabe, H. Sugama and S. Ferrando-Margalet, *Phys. Rev. Lett.* **100**, 195002 (2008).
- [7] T.-H. Watanabe, H. Sugama and S. Ferrando-Margalet, *Nucl. Fusion* **47**, 1383 (2007).
- [8] S. Ferrando-Margalet, H. Sugama and T.-H. Watanabe, *Phys. Plasmas* **14**, 122505 (2007).
- [9] P. Xanthopoulos, F. Merz, T. Görler and F. Jenko, *Phys. Rev. Lett.* **99**, 035002 (2007).
- [10] H. Sugama, T.-H. Watanabe and S. Ferrando-Margalet, *Plasma Fusion Res.* **3**, 041 (2008).
- [11] T.-H. Watanabe and H. Sugama, *Nucl. Fusion* **46**, 24 (2006).
- [12] O. Motojima, N. Ohyaibu, A. Komori *et al.*, *Nucl. Fusion* **43**, 1674 (2003).
- [13] H. Yamada, A. Komori, N. Ohyaibu *et al.*, *Plasma Phys. Control. Fusion* **43**, A55 (2001).
- [14] T. Kuroda and H. Sugama, *J. Phys. Soc. Jpn.* **70**, 2235 (2001).
- [15] P. Xanthopoulos and F. Jenko, *Phys. Plasmas* **13**, 092301 (2006).
- [16] P. Xanthopoulos, W.A. Cooper, F. Jenko, Yu. Turkin, A. Runov and J. Geiger, *Phys. Plasmas* **16**, 082303 (2009).
- [17] H.E. Mynick, P. Xanthopoulos and A.H. Boozer, *Phys. Plasmas* **16**, 110702 (2009).
- [18] S.P. Hirshman and O. Betancourt, *J. Comput. Phys.* **96**, 99 (1991).
- [19] M.N. Rosenbluth and F.L. Hinton, *Phys. Rev. Lett.* **80**, 724 (1998).
- [20] H. Sugama and T.-H. Watanabe, *Phys. Rev. Lett.* **94**, 115001 (2005).
- [21] H.E. Mynick and A.H. Boozer, *Phys. Plasmas* **14**, 072507 (2007).
- [22] A. Mishchenko, P. Helander and A. Könies, *Phys. Plasmas* **15**, 072309 (2008).
- [23] O. Yamagishi and S. Murakami, *Nucl. Fusion* **49**, 045001 (2009).
- [24] A.H. Boozer, *Phys. Fluids* **11**, 904 (1980).
- [25] S.P. Hirshman and R. Morris (ORNL), private communication.
- [26] M.A. Beer, S.C. Cowley and G.W. Hammett, *Phys. Plasmas* **2**, 2687 (1995).
- [27] E.A. Frieman and L. Chen, *Phys. Fluids* **25**, 502 (1982).
- [28] O. Yamagishi, M. Yokoyama, N. Nakajima and K. Tanaka, *Phys. Plasmas* **14**, 012505 (2007).
- [29] G. Rewoldt, L.-P. Ku, W.M. Tang, H. Sugama, N. Nakajima, K.Y. Watanabe, S. Murakami, H. Yamada and W.A. Cooper, *Nucl. Fusion* **42**, 1047 (2002).
- [30] T. Kuroda, H. Sugama, R. Kanno and M. Okamoto, *J. Phys. Soc. Jpn.* **69**, 2485 (2000).
- [31] H. Sugama and T.-H. Watanabe, *Phys. Plasmas* **13**, 012501 (2006).